SCIENTIFIC REPORTS
nature research

Check for updates

OPEN

New Synthesis Route for Complex Borides; Rapid Synthesis of Thermoelectric Yttrium Aluminoboride via Liquid-Phase Assisted Reactive Spark Plasma Sintering

Hyoung-Won Son[1,2], David Berthebaud[3], Kunio Yubuta[4], Akira Yoshikawa[4], Toetsu Shishido[4], Keiko Suzuta[5] & Takao Mori[1,2] ✉

$Y_xAl_yB_{14}$ ceramics are of high interest as high temperature thermoelectric materials with excellent p, n control. In this study, direct synthesis of dense polycrystalline $Y_xAl_yB_{14}$ ($x \sim 0.64$, $0.52 \leq y \leq 0.67$) ceramics was successfully carried out by spark plasma sintering using commercially available precursors. YB_4, AlB_2 and B powders were reactively sintered with an additive AlF_3 at 1773 K for 5–60 min in reduced Ar atmosphere. The sinterability was remarkably enhanced by liquid phase sintering comparing to conventional synthesis techniques. Phase composition analysis by X-ray diffraction showed that main peaks belong to $Y_xAl_yB_{14}$ with the $MgAlB_{14}$ structure type and no peaks of AlF_3 were detected. The thermoelectric behavior was changed from p-type to n-type with increasing Al occupancy. Power factor and *ZT* values measured in this study were found to be in the same range as the best values previously reported. This original synthesis process is found to be less precursor-consuming as compared to previous synthesis processes, and strikingly, less time-consuming, as the synthesis time, is shortened from 8 h to 5 min for p-type and to 1 h for n-type. The total process time is shortened from ≥3 days to ~4–5 h. This discovery opens the door for more accessible synthesis of complex borides.

Thermoelectric materials utilize the solid state Seebeck effect and thereby can directly convert heat to electricity. This energy harvesting technique has some advantages such as reliability, simplicity, environmental-friendliness, and so on. Thermoelectric performance is determined by the dimensionless figure of merit, $ZT = S^2\sigma T/\kappa$, where S is Seebeck coefficient, σ is electrical conductivity, T is absolute temperature, and κ is thermal conductivity. However, since S, σ and κ are basically in trade-off relationships, new approaches are required for breakthroughs[1–5].

Recently, an important topic is to develop energy harvesting technologies to power IoT (Internet of Things) sensors and devices[6,7]. For such a goal, organic, organic-inorganic hybrid, and inorganic materials are being developed to use near room temperature as flexible or micro-sized thermoelectric power generation modules[8,9].

On the other hand, at the other extreme of very high temperatures above 1000 K, there are various attractive high temperature thermoelectric applications. Namely, topping cycle for power plants, steelworks, industrial furnaces, etc[10–14]. In order to be used at such high temperatures, the materials need to possess robust high

[1]WPI International Center for Materials Nanoarchitechtonics (WPI-MANA), National Institute for Materials Science (NIMS), Namiki 1-1, Tsukuba, 305-0044, Ibaraki, Japan. [2]Graduate School of Pure and Applied Sciences, University of Tsukuba, Tennoudai 1-1-1, Tsukuba, 305-8671, Ibaraki, Japan. [3]CNRS-Saint Gobain-NIMS, UMI 3629, Laboratory for Innovative Key Materials and Structures (LINK), National Institute for Materials Science, Tsukuba, 305-0044, Ibaraki, Japan. [4]Institute of Multidisciplinary Research for Advanced Materials, Tohoku University, 2-1-1, Katahira, Aoba-ku, Sendai, 980-8577, Miyagi, Japan. [5]Nanotechnology Innovation Station, National Institute for Materials Science (NIMS), Namiki 1-1, Tsukuba, 305-0044, Ibaraki, Japan. ✉e-mail: MORI.Takao@nims.go.jp

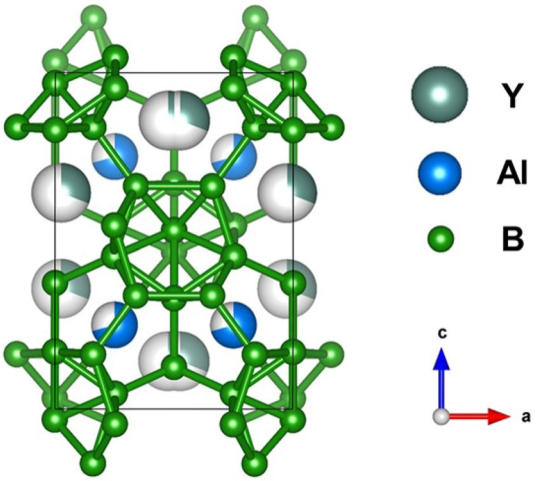

Figure 1. Depiction of crystal structure of $Y_xAl_yB_{14}$, first reported by Korsukova *et al.*[42], which is orthorhombic structure belonging to *Imma* space group. The boron atoms B1, B3, B4 and B5 form B_{12} icosahedra structures, which are interconnected via external B-B bonds or via B2 atom. Y and Al atoms partially occupy interstitial positions in the rigid three-dimensional B network.

temperature stability. Suitable material groups for such applications are refractory ceramics like oxides[15–20], nitrides[21,22], and borides. For the borides, investigations have been particularly carried out on such boron icosahedral compounds such as boron carbide[23–27], β-rhombohedral boron[28,29], $B_{12}As_2$[30,31], $RB_{44}Si_2$[32,33], RB_{66}[34,35], MB_6[36,37], R-B-C (N) compounds[38–40], and so on. One big issue for the borides is the difficulty of finding matching p-type and n-type compounds. The aforementioned compounds are predominantly p-type, with the exception of certain doped elements into beta-boron which have yielded n-type characteristic in a certain temperature range, and the R-B-C (N) compounds which are of interest as n-type counterparts to boron carbide[38–41].

$Y_xAl_yB_{14}$with orthorhombic structure[42], has been found to exhibit p- and n-type characteristics. Y and Al atoms partially occupy interstitial sites among B_{12} icosahedra clusters as shown Fig. 1. The thermoelectric behavior is changed from p-type to n-type by controlling Al occupancy. $Y_xAl_yB_{14}$ also has high melting point and excellent hardness, and thus, it is expected to be a promising candidate for high temperature thermoelectric applications[41,43–46].

Maruyama *et al.* and Sahara *et al.*[43–46]. have reported thermoelectric properties and microstructure of polycrystalline $Y_xAl_yB_{14}$ ceramics with a various range of Al occupancy. $Y_{0.57}Al_yB_{14}$ samples were synthesized with excess Al (y = 2.8–5.6) serving as flux, by sintering in induction furnaces for 8–12 h at 1400–1500 °C. To prepare dense bulk samples, the synthesized samples were pulverized, washed in NaOH solution, dried, and then sintered again by the spark plasma sintering (SPS) technique. SPS, which is one of the advanced sintering techniques, is effective for densification. In comparison with conventional sintering, SPS has some advantages such as rapid heating, shorter process time and densification at relatively lower temperatures[47–49].

However, in spite of using SPS, relative densities of obtained n-type $Y_xAl_yB_{14}$ ($x = \sim 0.56$; $0.57 \leq y \leq 0.63$) samples exhibited quite low values (71.1–89.4%) due to the material's poor sinterability. Furthermore, the previous synthesis method required a waste of resources by evaporation of large amounts of Al during the synthesis, and more importantly also requiring a complicated and time consuming total process[43–46]. This synthesis issue can be said to be a problem for many complex borides discovered with interesting electrical, magnetic, thermoelectric, and mechanical properties[50–54]. It is thus needed to develop a new, simple and reasonable synthesis process.

Recently, for synthesis and sintering of materials, which have poor sinterability, reactive SPS techniques and development of sintering additives have been studied. Son *et al.*[55] reported about fabrication of translucent AlN by SPS with MgF_2, which was used as a sintering additive. In general, AlN is also difficult to attain full densification due to its high covalent bonding. In that study, the liquid phase formed by MgF_2 assisted sintering, and as a result, fully densified and translucent samples were obtained with short sintering time (20 min). Densification of complex borides which do not melt stably and have an upper limit on temperatures which can be used for sintering, are an even more difficult problem. For example, different sintering conditions[39,56] and sintering aids were tried for the metal borocarbonitrides which are attractive thermoelectric materials, with some effective sintering aids found, but which were detrimental to the properties.

In this study, a new approach with reactive SPS is investigated to synthesize and prepare dense n-type $Y_xAl_yB_{14}$ ceramics. As a new sintering additive, AlF_3 is used. It is expected that AlF_3 can enhance sinterability by forming a liquid phase during sintering due to its relatively low melting point.

Results and Discussion

Figures 2 and 3 show the XRD patterns measured on the surface of YA0 composition samples sintered with and without AlF_3 at 1773 K, respectively. The XRD pattern of sample sintered for 10 min without AlF_3 exhibits numerous peaks of secondary phases such as unreacted YB_4, YB_6, YB_{12}, α-alumina, and so on, as shown in Fig. 2. The peaks of secondary phases are still detected on the YA0 composition sample which were even sintered for 1 h. It means that the reaction for synthesis of $Y_xAl_yB_{14}$ is independent on sintering time in this case.

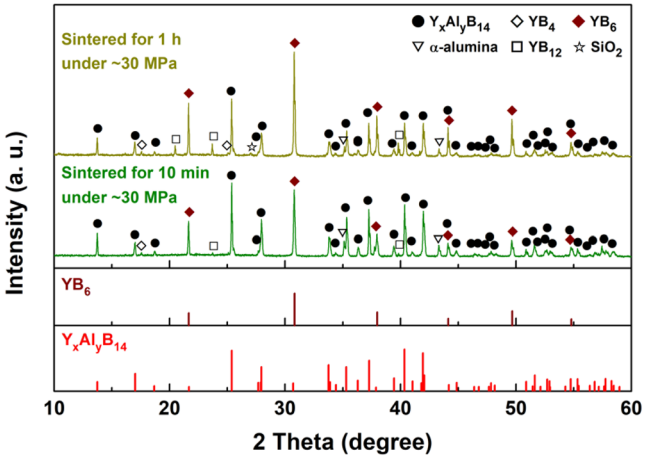

Figure 2. XRD patterns of YA0 composition ($Y_{0.62}Al_{0.71}B_{14}$) samples prepared by reactive SPS without AlF_3 addition. The samples were sintered at 1773 K under uniaxial pressure of ~30 MPa in a reduced Ar atmosphere for 1 h and 10 min, respectively. The standardized intensities for $Y_xAl_yB_{14}$ and YB_6 are shown with sample's XRD patterns.

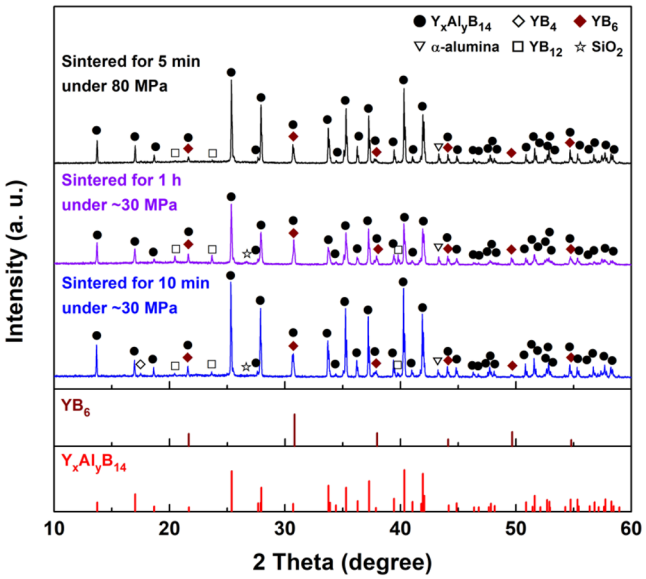

Figure 3. XRD patterns of YA0 composition ($Y_{0.62}Al_{0.71}B_{14}$) samples prepared by reactive SPS with AlF_3 addition. The samples were sintered at 1773 K in a reduced Ar atmosphere for 1 h and 10 min under the uniaxial pressure of ~30 MPa, and for 5 min under the uniaxial pressure of 80 MPa, respectively. The standardized intensities for $Y_xAl_yB_{14}$ and YB_6 are shown with sample's XRD patterns.

In contrast, the XRD patterns of the same composition samples sintered with AlF_3 at the same sintering condition exhibit relatively much less peaks of secondary phases, and no peak of AlF_3 was detected. It implies that AlF_3 dramatically improved the reactivity among starting materials by liquid phase sintering, and then was completely removed without remaining by evaporation under the reduced Ar atmosphere. The relatively purest $Y_xAl_yB_{14}$ was obtained for the sample sintered for 5 min under the uniaxial pressure of 80 MPa with AlF_3 (Fig. 3). Although some peaks of α-alumina and YB_6 phases are still detected as in the previous conventional synthesis studies[43,44], polycrystalline $Y_xAl_yB_{14}$ was successfully synthesized via reactive SPS with AlF_3.

The axial displacement changes of the YA0 composition samples during SPS are shown in Fig. 4. The temperature at the minimum displacement indicates the starting initial stage of sintering. In the case of the sample sintered without AlF_3 under ~30 MPa which is the minimum pressure of SPS, the shrinkage was started at ~1550 K but densification was not finished even at 1773 K. On the other hand, in the case of the sample sintered with AlF_3 under ~30 MPa, the shrinkage was started at ~1450 K and densified well during heating process. This result suggests that the sinterability and densification behavior were remarkably improved by AlF_3. The melting point of AlF_3 is ~1573 K at 1 atm. This temperature is higher than that for the starting shrinkage (~1450 K). It is therefore

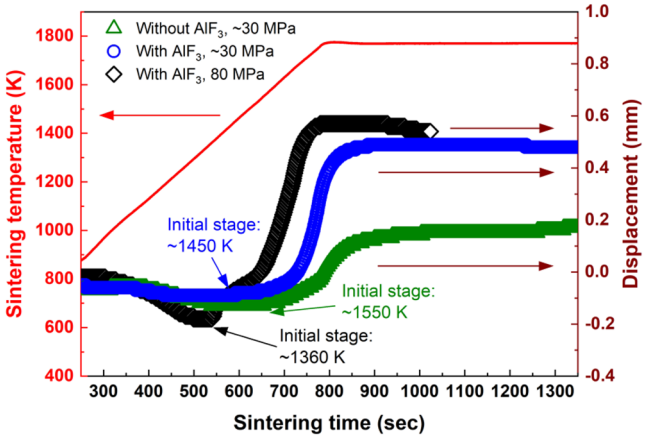

Figure 4. Densification behavior of $Y_xAl_yB_{14}$ sintered without AlF_3 under ~30 MPa, with AlF_3 under ~30 MPa and with AlF_3 under 80 MPa. To investigate the effect of AlF_3 to densification, same amount of mixture and same graphite die and spacers were used.

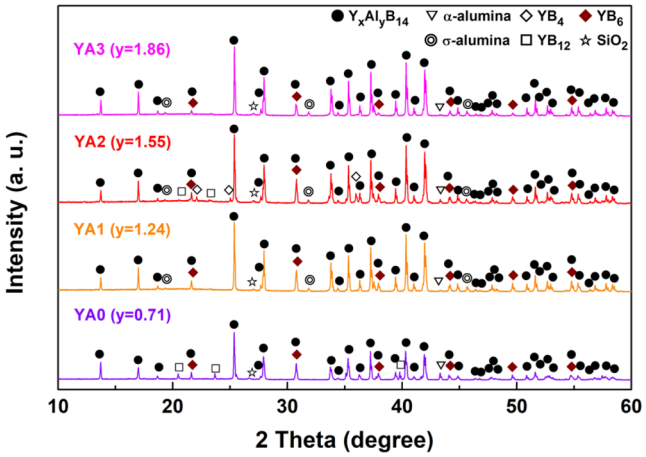

Figure 5. XRD patterns of YA0, YA1, YA2 and YA3 composition ($Y_{0.62}Al_yB_{14}$; y = 0.71–1.86) samples prepared by reactive SPS with AlF_3 addition. The samples were sintered at 1773 K under uniaxial pressure of ~30 MPa in a reduced Ar atmosphere for 1 h.

considered that the reduced-pressure Ar atmosphere lowered the melting point of AlF_3, and the initial stage was shifted earlier, namely ~100 K lower by formation of liquid phase of AlF_3.

The densification behavior of the YA0 composition sample sintered with AlF_3 under uniaxial pressure of 80 MPa was further enhanced. The shrinkage of the pressure-assisted sample was started from ~1360 K, and the shrinkage rate was changed from ~1450 K. Since the temperature where shrinkage rate was changed is the same as the temperature of the starting initial stage of the sample sintered with AlF_3 under ~30 MPa, the shrinkage observed from 1360 to 1450 K indicates the effect of the applied pressure. All samples exhibited changes of shrinkage rate during the intermediate stage. These phenomena can be mainly attributed to the different shrinkage rate between the main phase and the secondary phases.

Figure 5 shows XRD patterns of $Y_{0.62}Al_yB_{14}$ samples (YA0–3; y = 0.71–1.86) sintered at 1773 K with AlF_3 for 1 h under ~30 MPa. Together with the prominent peaks of $Y_xAl_yB_{14}$, weak peaks of several secondary phases such as α-alumina, σ-alumina, YB_4, YB_6, YB_{12} and SiO_2 were detected. The Al-poor sample (YA0) exhibited peaks of α-alumina, YB_6, YB_{12} and SiO_2, whereas the Al-rich samples (YA1, YA2 and YA3) exhibited peaks of σ-alumina in addition. The structure of σ-alumina ($Al_{2.667}O_4$) is described as a defect cubic spinel in which Al cations randomly and partially occupy its octahedral and tetrahedral sites[57]. The result thus implies that addition of Al and reductive atmosphere affects formation of σ-alumina during sintering of Al-rich samples. For Al-rich samples, the intensity of the detected YB_6 and YB_{12} peaks decreased with increasing Al content. It indicates that the excess Al compensated the Al loss caused by the formation of alumina phase during sintering. Relatively homogeneous yttrium aluminoborides were obtained for the YA3 composition. The XRD pattern for the YA2 sample shows the presence of YB_4. It is attributed to inhomogeneous mixing of starting materials. To obtain $Y_xAl_yB_{14}$ without secondary phases, such as SiO_2, YB_4, YB_6 and YB_{12}, optimization of the mixing process is required. We also found out that the SiO_2 in the XRD patterns of the samples came from the agate mortar, which was used to pulverize each

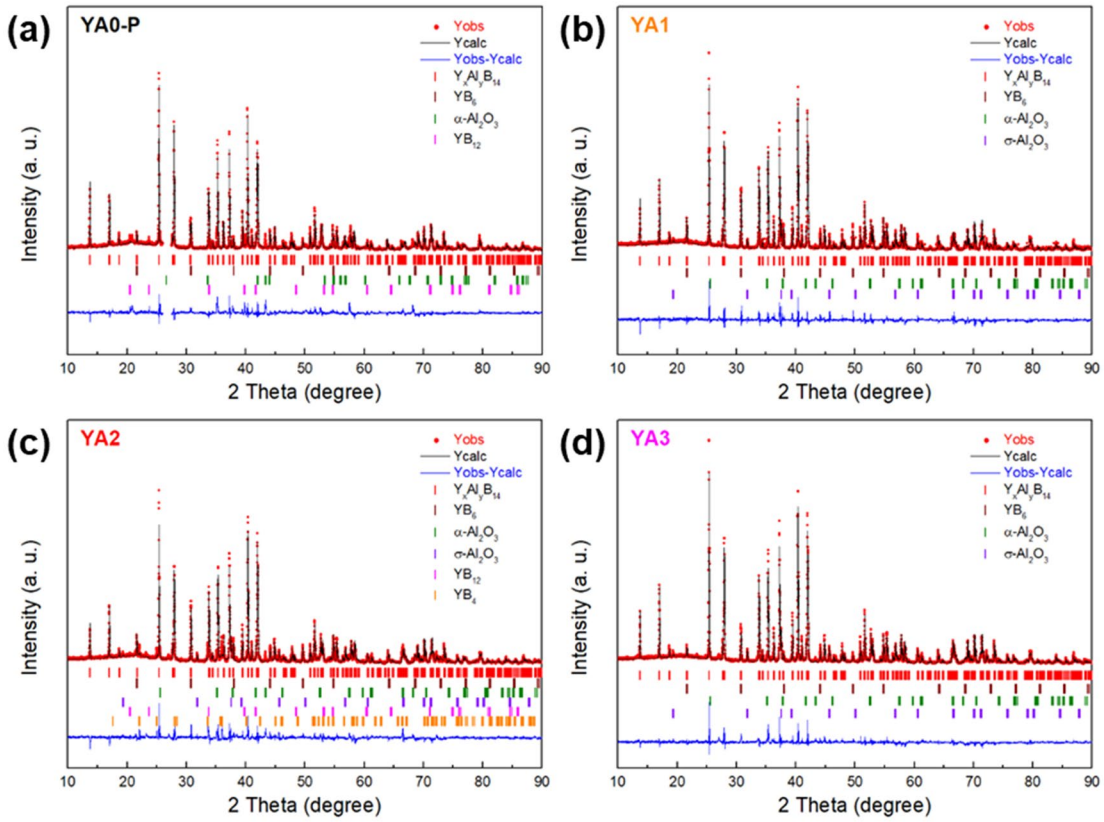

Figure 6. XRD pattern and the results of Rietveld refinement of YA0-P, YA1, YA2 and YA3 samples prepared by reactive SPS with AlF_3 addition. The YA0-P sample was sintered at 1773 K for 5 min under 80 MPa, whereas the YA1, YA2 and YA3 samples were sintered at 1773 K for 60 min under ~30 MPa.

Sample name	Starting composition	Sintering conditions (Temperature × time)	Pressure (MPa)	Atmosphere
YA0-P	$Y_{0.62}Al_{0.71}B_{14}$	1773 K × 5 min	80	Ar
YA1	$Y_{0.62}Al_{1.24}B_{14}$	1773 K × 60 min	~30	Ar
YA2	$Y_{0.62}Al_{1.55}B_{14}$	1773 K × 60 min	~30	Ar
YA3	$Y_{0.62}Al_{1.86}B_{14}$	1773 K × 60 min	~30	Ar

Table 1. The synthesis conditions of $Y_xAl_yB_{14}$ samples.

sample before powder XRD measurement. This was indicated because the intensity of the peak at $2\theta = 26–27°$ increased with increasing pulverization time.

The fractional occupancies of x and y, of Y and Al, in the Al-poor (YA0-P) and -rich samples (YA1, YA2 and YA3) prepared by reactive SPS with AlF_3 were estimated from Rietveld refinement within the technique limit (Fig. 6). At first starting atom position from Korsukova *et al.*[42] model was used to perform refinements. Ultimately, atom positions were refined, together with partial occupancies for Y and Al positions. The synthesis conditions and the results of Rietveld refinement of each sample are summarized in Table 1 and Table 2, respectively. The refined Y contents (x in $Y_xAl_yB_{14}$) of all samples are ~0.64, which is almost the same value as that of the starting materials. This result implies that no Y loss during reactive SPS occurred. The refined Al content (y in $Y_xAl_yB_{14}$) of YA0-P is 0.52 though the starting content was 0.71. It suggests that Al was evaporated during sintering due to high sintering temperature and reduced Ar atmosphere. Meanwhile, the refined Al contents of YA1, YA2 and YA3 are ~0.67, which are much less than their initial Al contents (1.24, 1.55 and 1.86). Since these compositions are quite similar to those determined from single crystal x-ray diffractometry $Y_{0.62}Al_{0.71}B_{14}$[42], it is considered that the Y and Al atoms occupy their interstitial sites as maximumly as possible to satisfy the 4 electron deficient nature[53,54], and thus excess Al could not occupy Al sites.

The phase fractions and the theoretical and relative density of each sample are given in Table 3. At around 5%, the largest impurity phase is the alumina phase. We have tried to remove it but intrinsically find that it is difficult. As raw materials, amorphous boron is used for many sintering synthesis of complex borides which are difficult to synthesize by simple arc melting, for example[54]. There is some oxidation of the sensitive amorphous boron and in combination with aluminum for the present compound, alumina is formed. We tried to remove the oxygen

Sample name	Starting composition	Refined composition	a (Å)	b (Å)	c (Å)	Volume of lattice (Å^3)
YA0-P	$Y_{0.62}Al_{0.71}B_{14}$	$Y_{0.66}Al_{0.52}B_{14}$	5.825	10.401	8.205	497.107
YA1	$Y_{0.62}Al_{1.24}B_{14}$	$Y_{0.64}Al_{0.67}B_{14}$	5.812	10.416	8.190	495.805
YA2	$Y_{0.62}Al_{1.55}B_{14}$	$Y_{0.62}Al_{0.66}B_{14}$	5.811	10.414	8.188	495.503
YA3	$Y_{0.62}Al_{1.86}B_{14}$	$Y_{0.65}Al_{0.67}B_{14}$	5.811	10.413	8.189	495.516

Table 2. Compositions and lattice parameters of sintered samples, which were estimated from Rietveld analysis.

Sample name	$Y_xAl_yB_{14}$ (wt.%)	YB_6 (wt.%)	α-Al_2O_3 (wt.%)	σ-Al_2O_3 (wt.%)	YB_{12} (wt.%)	YB_4 (wt.%)	Theoretical density (g/cm^3) (Relative density (%))
YA0-P	91.53	1.30	6.33	—	0.85	—	3.09 (96.1%)
YA1	92.65	2.52	0.16	4.67	—	—	3.08 (100%)
YA2	91.15	2.41	0.21	4.04	0.00	2.19	3.08 (98.7%)
YA3	93.07	0.89	0.15	5.89	—	—	3.08 (99.7%)

Table 3. Phase fraction of constituent phases and theoretical and relative density of each sample. The phase fraction of constituent phases and theoretical densities are estimated using Rietveld refinement.

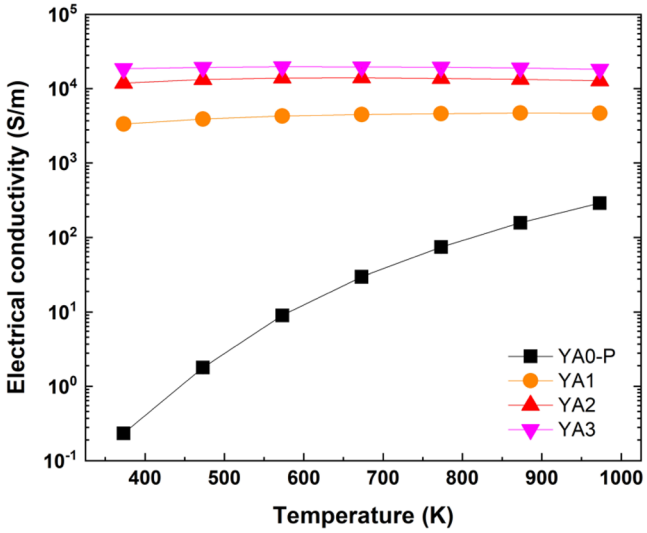

Figure 7. Temperature dependence of logarithmic electrical conductivities of Al-poor (YA0-P) and -rich samples (YA1, YA2 and YA3) prepared by reactive SPS. The YA0-P sample was sintered at 1773 K for 5 min under 80 MPa, whereas the YA1, YA2 and YA3 samples were sintered at 1773 K for 60 min under ~30 MPa. Error bars represent a measurement uncertainty range (±7%).

by heating the amorphous boron and evaporation of BO, but found that handling in air, the amorphous boron is easily oxidized again. Therefore, in this case, the alumina impurity phase is intrinsically difficult to eliminate. However, together with metallic YB_6, etc. which typically appear since mixing is generally not ideal, it is indicated that these secondary phases do not have a significant effect on the thermoelectric properties, as discussed below.

The temperature dependence of electrical conductivities for Al-poor (YA0-P) and -rich samples (YA1, YA2 and YA3) prepared by reactive SPS is shown in Fig. 7. At the low temperature region, the Al-poor sample exhibits extremely low electrical conductivity compared to Al-rich samples. However, a particularly large increase of electrical conductivity is observed with increasing temperature due to its conducting mechanism which will be described below. On the other hand, all the Al-rich samples exhibit several orders higher electrical conductivities. The highest electrical conductivity values are obtained for YA3 sample which is ~5 times higher than that of the YA1 sample. We consider the possibilities of the secondary phases having any effect on the thermoelectric properties. Amongst the thermoelectric properties, the electrical conductivity can be considered to have the potential to be most sensitive to small amounts of metallic phases or insulating phases, considering that these phases may have orders different resistivity than the main material. As an illustrative example we compare YA1 and YA3. From the Rietveld analysis, the composition (Table 2) and phase fraction (Table 3) of the main $Y_xAl_yB_{14}$ phase is quite similar, as are the relative densities of the samples which are both close to 100% (Table 3). YA1 has a significantly larger amount of metallic YB_6 impurities and also slightly less amount of insulating alumina impurities compared to YA3. However, as noted above, the conductivity of YA1 is actually around 5 times lower than

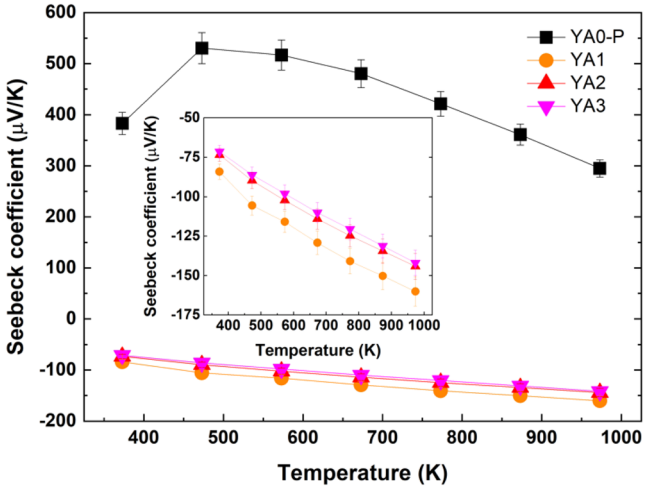

Figure 8. Temperature dependence of Seebeck coefficients of Al-poor (YA0-P) and -rich samples (YA1, YA2 and YA3) prepared by reactive SPS. The YA0-P sample was sintered at 1773 K for 5 min under 80 MPa, whereas the YA1, YA2 and YA3 samples were sintered at 1773 K for 60 min under ~30 MPa. The Seebeck coefficients of Al-rich samples are shown in the inset. Error bars represent a measurement uncertainty range (±7%).

YA3, indicating that the secondary phases in this case are not having a significant effect on the thermoelectric properties.

We consider the origin of the difference in properties. The large difference between YA1 and YA3 is only the starting composition (Table 2), where the amount of initial excess Al is around 1.5 times higher for YA3. Since Al itself cannot be seen in the XRD patterns, we speculate that Al atoms may be seeded in the grain boundaries and result in an enhancement of the electrical conductivity. Such an effect has been proposed before[58] and observed in Ba seeding of $Ca_3Co_4O_9$ for example[59].

Figure 8 shows the temperature dependence of Seebeck coefficients for each sintered sample. The Seebeck coefficient of Al-poor sample exhibits positive values, whereas those of Al-rich samples exhibit negative values. This indicates that the thermoelectric behavior of $Y_xAl_yB_{14}$ samples are changed from p-type to n-type with increasing Al occupancy. The Seebeck coefficient values for Al-poor sample increases up to 473 K, and then decreases with increasing temperature. In contrast, the absolute values of negative Seebeck coefficients for Al-rich samples increase with increasing temperature. The maximum positive and negative values, 530 μV/K and −160 μV/K, are obtained for YA0-P at 473 K and for YA1 at 973 K, respectively.

Figure 9(a,b) show the temperature dependence of electrical conductivity of each sintered sample in accordance with thermally activated conduction (TAC) mode and variable range hopping (VRH) mode, respectively. According to the TAC model, the conductivity is expressed as the following;

$$\sigma_{TAC} = \sigma_{0,TAC}\exp\left(-\frac{E_A}{kT}\right) \quad (1)$$

Meanwhile, in disordered systems, according to the VRH model, the conductivity for three dimensional systems is given by

$$\sigma_{VRH} = \sigma_{0,VRH}\exp\left(-\frac{T_0}{T}\right)^{\frac{1}{4}} \quad (2)$$

where $\sigma_{0,TAC}$ and $\sigma_{0,VRH}$ are constants which do not depend on temperature, E_A is the thermal activation energy, T_0 is the characteristic temperature determined by the density of localized states near the Fermi level, k is the Boltzmann's constant and T is the absolute temperature[60].

We consider the validity of the two different conduction models for our samples. In Fig. 9(a), the temperature dependence of the electrical conductivity of the Al-poor sample appears to generally follow the TAC dependence, except it appears to deviate from a straight line below 573 K. In contrast, in Fig. 9(b), the temperature dependence of the electrical conductivity appears to not be as good a fit to the VRH dependence as it shows a curvature over a wider temperature range. This implies that TAC is the dominant conduction mechanism for Al-poor $Y_xAl_yB_{14}$ above 573 K. In this case, the calculated E_A and $\sigma_{0,TAC}$ from the fitted line are 0.4 eV and 3.95×10^4 S/m, respectively. This activation energy value is similar to the band gap energy in the result of band structure calculation for $Y_{0.50}Al_{0.75}B_{14}$[45].

We will consider the mechanism for the low temperature deviation below together with the discussion on the Seebeck coefficient. For Al-rich samples, neither the TAC (Fig. 9(a)) or VRH (Fig. 9(b)) is a good fit, with the rate of increase of the electrical conductivity apparently suppressed at higher temperatures. We speculate that the reason of this suppression may be due to the presence of the Al segregation. This effect only appears to be noticeable for the highest conductive samples (i.e. Al-rich samples at high temperatures) and does not appear to be

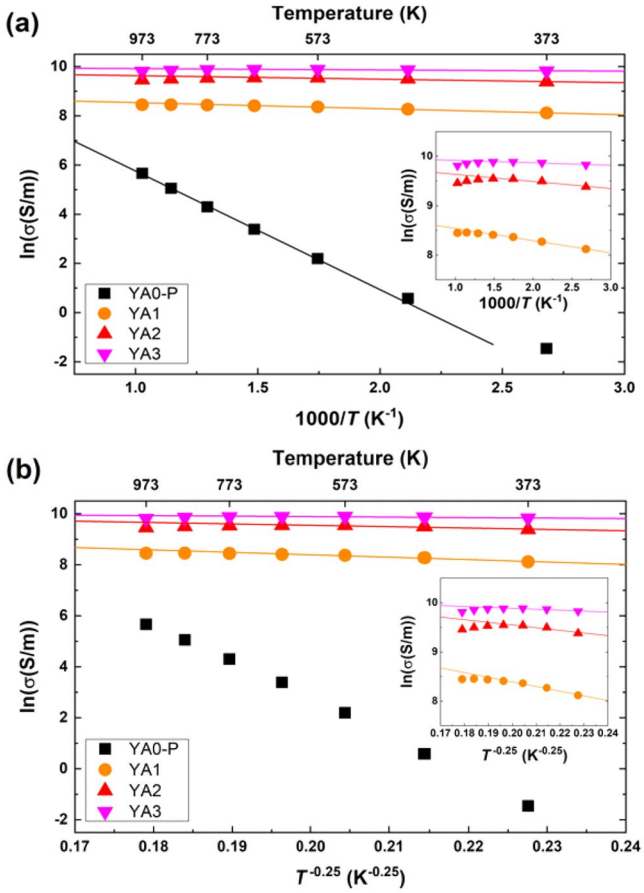

Figure 9. Temperature dependence of electrical conductivity of each sintered sample. The lnσ is plotted versus (**a**) T^{-1} for TAC mode and (**b**) $T^{-0.25}$ for VRH mode, respectively. The straight line for Al-poor sample in TAC mode expresses the fit to Eq. 1 for the temperature range from 573 K to 973 K. Also, the straight lines for Al-rich samples in TAC mode and VRH mode express the fit to Eq. 1 and to Eq. 2 for the temperature range from 373 K to 673 K, respectively.

pronounced for the Al-poor sample where the level of electrical conductivity is much lower to begin with. For the Al-rich samples we attempt to obtain insight on the conduction mechanism through the temperature dependence of the Seebeck coefficient discussed below.

The temperature dependences of Seebeck coefficients for TAC and VRH are shown in Fig. 10. When the carrier concentration is increased by thermal activation, the Seebeck coefficient is generally expressed as the following[61,62];

$$S = -\left(\frac{k}{e}\right)\left(\frac{E_s}{kT} + A\right) \tag{3}$$

where e is carrier charge, k is Boltzmann constant, E_s is the characteristic carrier-generation energy, T is the absolute temperature, and A is the heat-of-transport constant. However, the plots of Seebeck coefficients of all samples do not appear to have a clear T^{-1} component, not only for n-type but also for p-type $Y_xAl_yB_{14}$ (Fig. 10(a)) which generally follows TAC for the electrical conductivity as discussed above.

The reason can be elucidated by considering the mixed conduction case in semiconductors. In that case, the total Seebeck coefficient is given by[61]

$$S = \frac{(S_n\sigma_n + S_p\sigma_p)}{(\sigma_n + \sigma_p)} \tag{4}$$

where σ_n and σ_p are the electrical conductivity due to electrons and holes, and S_n and S_p are the Seebeck coefficient for n-type and p-type conduction, respectively. Considering the temperature dependence of electrical conductivity discussed above, namely, the deviation to higher electrical conductivity at higher temperatures, the decrease of Seebeck coefficient of the Al-poor YA0-P above 573 K can therefore be attributed to the increase of thermally excited electrons.

In VRH systems, the temperature dependence of the Seebeck coefficient can be approximated by the following[62];

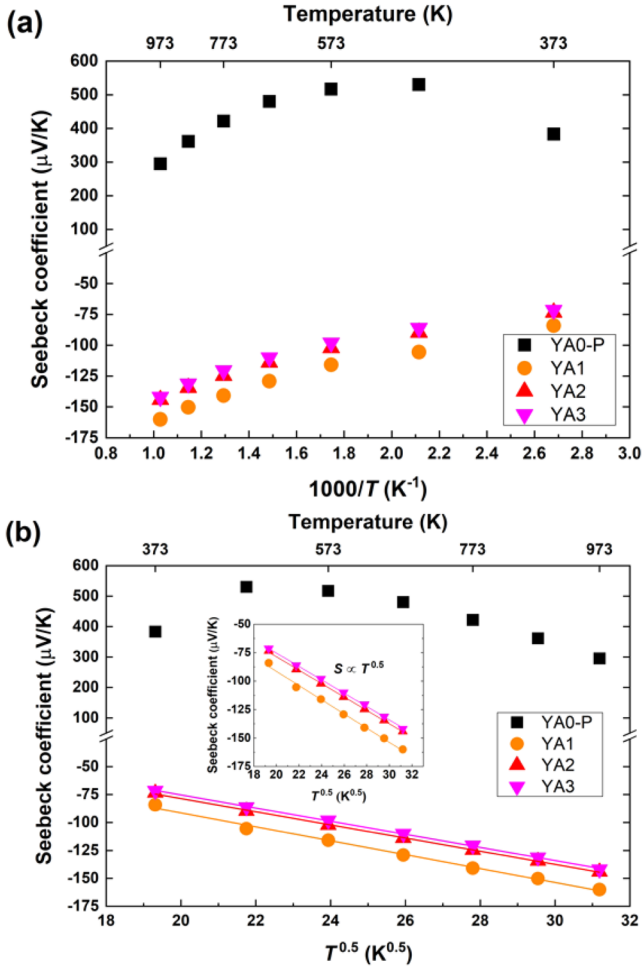

Figure 10. Temperature dependence of the Seebeck coefficients of all samples in accordance with (**a**) TAC mode and (**b**) VRH mode. The inset shows the Seebeck coefficients of Al-rich samples in accordance with VRH mode. The straight lines for Al-rich samples in VRH mode express the fit to Eq. 5 for the temperature range from 373 K to 973 K.

$$S \propto (T_0 T)^{\frac{1}{2}} \left(\frac{d \ln N(E)}{dE} \right)\Big|_{E=E_F} \quad (5)$$

where N(E) is the density of states at the Fermi level. For Al-rich samples, the temperature dependence of the Seebeck coefficients is almost proportional to $T^{0.5}$, as shown in Fig. 10(b). From this temperature dependence of the Seebeck coefficient it is indicated that the Al-rich samples are VRH systems, since insulating or metallic impurities have less effect on the Seebeck coefficient.

To summarize what we have concluded from the data, the conduction mechanism of the Al-poor sample appears to follow TAC dependence, with deviations in the temperature dependences above 573 K indicated from thermally excited electrons. With the large increase of Al inserted atoms, and thereby electrons, for the Al-rich samples, not to mention a speculated effect of excess segregated Al atoms for YA3 in particular, the magnitude of electrical conductivity increases greatly compared to the Al-poor sample. However, despite this, it is indicated that the conduction mechanism follows the VRH mechanism, indicating that the electrical carriers have some localization due to disorder.

Figure 11 shows the densities of the sintered bodies measured by Archimedes' method. All samples prepared by reactive SPS exhibit rather high densities, 2.97–3.07 g/cm^3, compared to that of the reference sample (2.43 g/cm^3)[44], and are close to the theoretical density of the single crystal $Y_{0.62}Al_{0.71}B_{14}$, 3.02 g/cm^3. The measured densities for Al-rich samples are a little bit higher than the reported theoretical density of single crystal due to the presence of secondary phases. However, even taking into consideration the presence of a relatively small amount of secondary phases, highly dense samples were obtained (Table 3). This result suggests that the new synthesis process via reactive SPS with AlF_3 is also much more effective for densification of yttrium aluminoboride than the conventional process.

The thermal conductivities of n-type $Y_xAl_yB_{14}$ samples are shown in Fig. 12. Thermal conductivities generally decrease with increasing temperature indicating Umklapp scattering. YA2 and YA3 show some difference in the

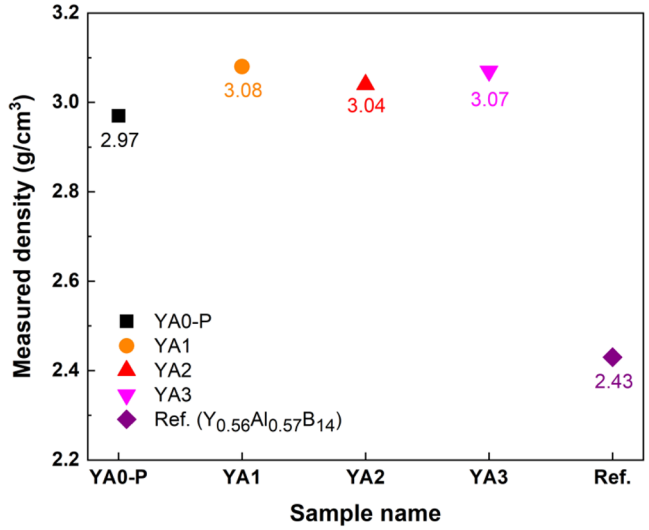

Figure 11. Measured densities of as-sintered $Y_xAl_yB_{14}$ (x~0.64) samples, which are compared with the reported value of $Y_{0.56}Al_{0.57}B_{14}$[44]. The theoretical and relative densities of the samples prepared by reactive SPS in the present study are given in Table 3.

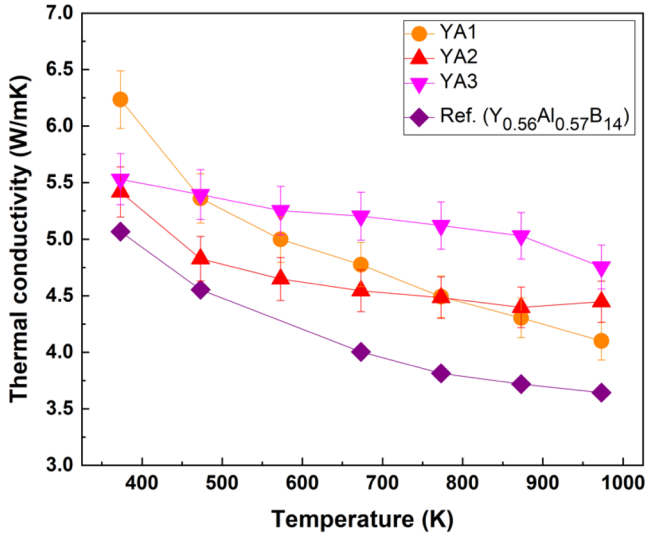

Figure 12. Thermal conductivities of n-type $Y_xAl_yB_{14}$ (x ~0.64) samples prepared by reactive SPS, which are compared with the reported value of $Y_{0.56}Al_{0.57}B_{14}$[44]. Error bars represent a measurement uncertainty range (±5%).

temperature dependence, with relatively less temperature dependence compared to YA1 and YA0-P. This trend is also reflected to a lesser extent in the intrinsic thermal diffusivities (Fig. S1). The behavior may be due to the Al segregation speculated before, since both YA2 and YA3 have higher Al starting compositions, but it is not clear at present. In comparison to reported samples, all samples exhibit slightly higher thermal conductivities due to their relatively higher densities than what has previously been obtained.

To investigate the microstructure, SEM observation for fracture surface of the samples was carried out (Fig. 13). The samples synthesized by reactive SPS exhibit highly dense microstructure compared to that of previous samples[46] though a minor amount of small pores are observed. All samples show coarse microstructure due to the high sintering temperature and liquid phase introduced during sintering. The microstructures generally consist of two phases, which are observed as a dark region and a bright region. The components in both regions are revealed by EDX analysis, as shown in Fig. 14. The result shows the presence of main elements, Y, Al, B and O. The dark region contains Y, Al and B but not O, whereas the bright region contains Al and O but not Y and B. It thus can be considered that the matrix and the secondary phase are $Y_xAl_yB_{14}$ and alumina, respectively. In the matrix phase, some differences in the contrast are observed. It implies an inhomogeneity of the metal atoms which occupy the interstitial sites in $Y_xAl_yB_{14}$. Standard molar enthalpy of formation (ΔH_f^0) and standard molar entropy (S^0) of each material are listed in Table 4[63]. The calculated free energies of formations (ΔG^0) for AlB_2,

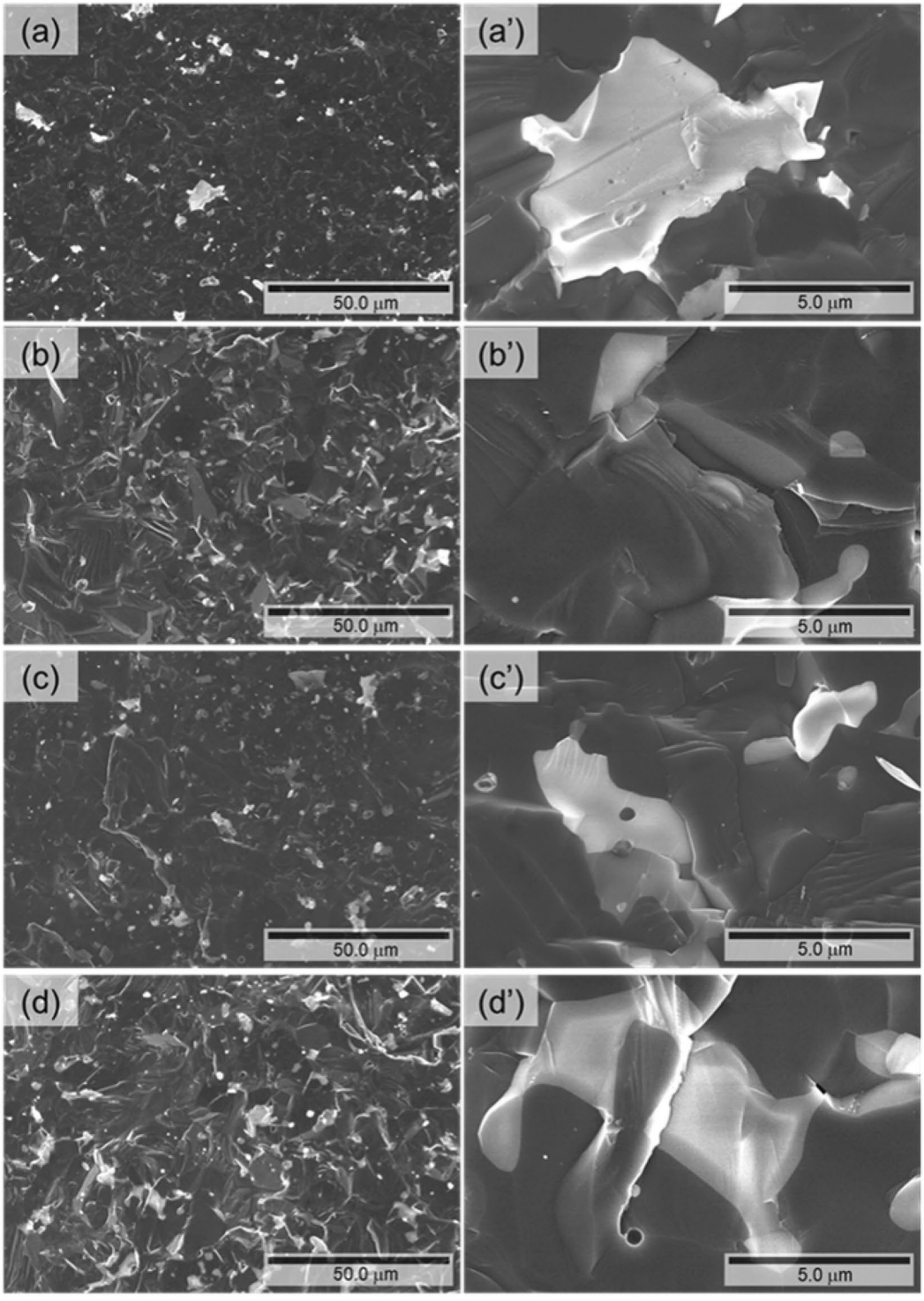

Figure 13. SEM images of fracture surface for $Y_xAl_yB_{14}$ samples prepared by reactive SPS, (**a,a'**) YA0-P, (**b,b'**) YA1, (**c,c'**) YA2 and (**d,d'**) YA3.

Al_2O_3 and B_2O_3 were listed and plotted, as shown in Table 5 and Fig. 15[64]. The results of thermodynamic calculations show that ΔG^0 of α-alumina is much lower than AlB_2 and B_2O_3. As discussed previously, it is considered that the presence of boron oxide layer coated on the surface of particles of the starting material of amorphous boron reacted with Al during sintering, and thus the alumina phase was formed. We have found that even after removing the boron oxide by the pre-treatment of heating, the amorphous boron powder can have oxidation in air again. To suppress the formation of alumina phase, using a closed system to enable heating of the raw material amorphous boron and then continuously, the mixing process and SPS sintering is desirable.

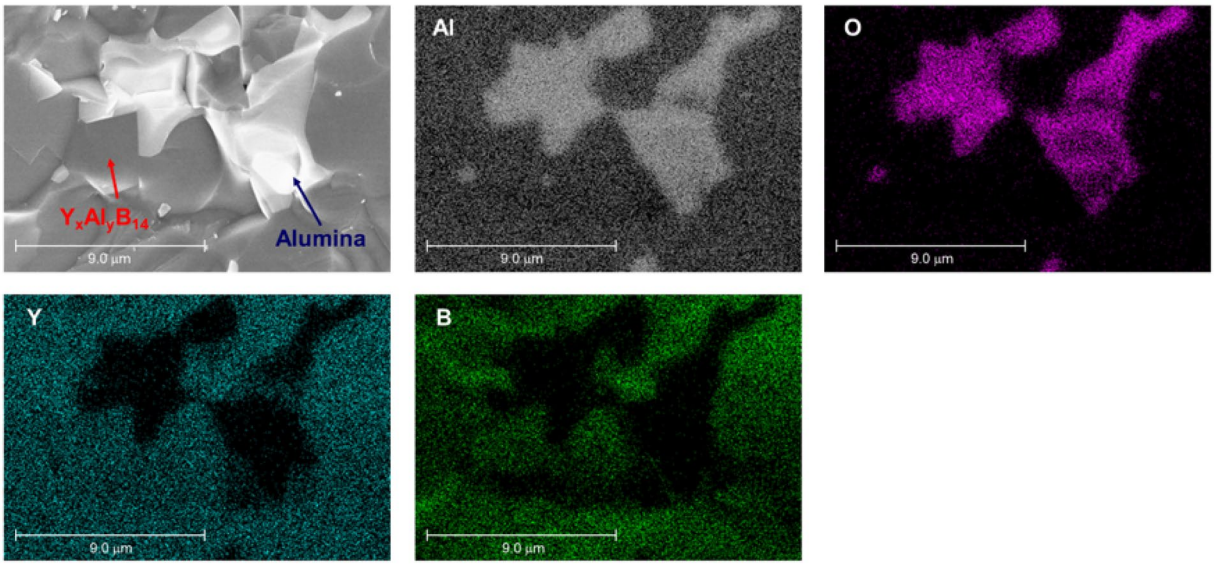

Figure 14. The result of EDX analysis on the microstructure in fracture surface of YA1. The distribution of Y, Al, B and O atoms were investigated by the mapping technique.

Material	ΔH_f^0 (kJ/mol)	S^0(J/molK)
O_2 (*g*)	0	205.15
B (*s*)	0	5.9
Al (*s*)	0	28.3
Al_2O_3 (*s*)	−1675.7	50.92
AlB_2 (*s*)	−151	34.7
B_2O_3 (*s*)	1273.5	53.97

Table 4. Standard molar enthalpies of formation and standard molar entropies at 298 K[63].

Reaction	Gibbs free energy of formation (J/mol)
$Al(s) + 2B(s) \rightarrow AlB_2(s)$	$\Delta G^0 = -151 + 0.0054\,T$
$2Al(s) + 3/2O_2(g) \rightarrow Al_2O_3(s)$	$\Delta G^0 = -1675.7 + 0.3134\,T$
$2B(s) + 3/2O_2(g) \rightarrow B_2O_3(s)$	$\Delta G^0 = -1273.5 + 0.2420\,T$

Table 5. Gibbs free energy of formation changes accompanied by each reactions.

Figure 16(a,b) show the power factors and *ZT* values of $Y_xAl_yB_{14}$ samples with the reference sample[44], respectively. The power factor is dramatically improved by increasing Al occupancy. The maximum power factor, 3.7×10^{-4} W/mK^2, was obtained for YA3 at 973 K, which is significantly higher than that of the reference $Y_{0.56}Al_{0.57}B_{14}$ sample(Fig. 16(a)). The large improvement in power factor can be attributed to the high density achieved by the new synthesis process. The maximum *ZT* value, 0.08 was also obtained for YA3, as shown in Fig. 16(b). This value is comparable with those reported by previous study, because of the higher thermal conductivity. However, looking forward, it can be said that in general it is more straightforward to find ways to selectively lower the thermal conductivity[65,66], rather than enhance the power factor[67,68], Although the *ZT* is not high, there are very few materials which potentially can be used for very high temperature thermoelectric applications[10], and we succeeded to prepare $Y_xAl_yB_{14}$ by developing a new sintering process, which is much shorter, simpler and more cost-effective.

Conclusions

In this study, a new synthesis process with SPS and sintering additive for synthesis of dense yttrium aluminoboride was developed. The addition of 1 wt.% AlF_3 effectively and dramatically enhanced the sinterability and densification behavior of yttrium aluminoboride by the formation of liquid phase during SPS. Consequently, the process was remarkably simplified and total process time was shortened from ≥3 days to only ~4–5 h.

For p-type $Y_xAl_yB_{14}$, the thermally activated conduction mechanism was proposed rather than the usually assumed variable range hopping (VRH) mechanism, to explain the experimental results of the temperature dependence of electrical conductivity and Seebeck coefficient. Conversely, the VRH mechanism appears to be a good match for the observed properties of the n-type $Y_xAl_yB_{14}$. Because of the increasing Al occupancy and

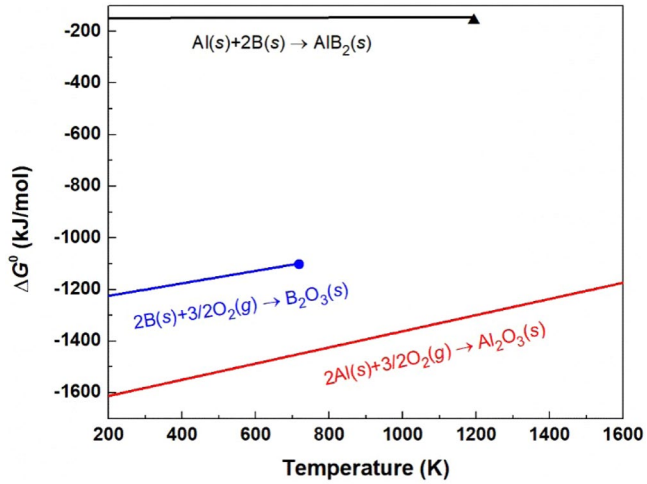

Figure 15. Gibbs free energy of formation of AlB_2, B_2O_3 and Al_2O_3 with temperature range. The point positioned at the end of B_2O_3 line indicates melting temperature of B_2O_3 (723 K), and the triangle positioned at the end of AlB_2 line indicates decomposition temperature (~1193 K)[64].

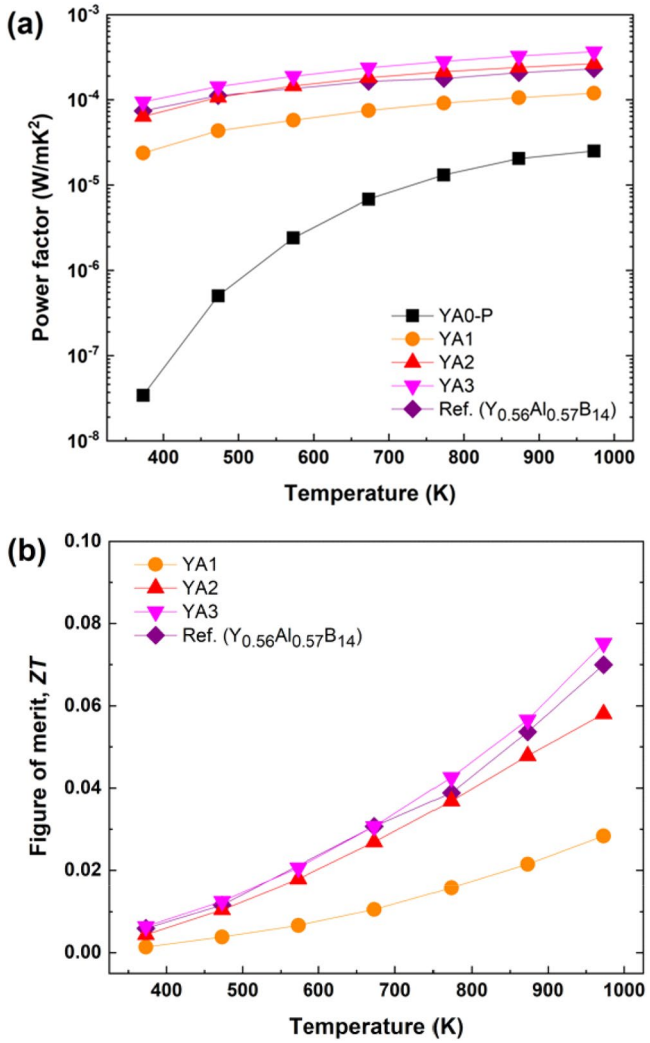

Figure 16. (**a**) Power factor and (**b**) figure of merits for $Y_xAl_yB_{14}$ (x ~0.64) samples prepared by reactive SPS, which are compared with the reported value of $Y_{0.56}Al_{0.57}B_{14}$[44].

thereby electron carrier content, the n-type samples have much higher conductivity, however, despite this it is indicated that the electrical carriers have some localization due to disorder. *ZT* values of yttrium aluminoboride prepared by reactive SPS exhibits overall similar thermoelectric properties as the previously reported best samples prepared by conventional processes. The power factor is significantly enhanced because of the high density achieved by the present discovered method. The higher thermal conductivity balances out the *ZT*, however, in thermoelectric research there are many methods to selectively lower the thermal conductivity. In any case, the present synthesis method that we discovered radically shortens the time necessary for synthesis, e.g. from 8 h to 5 min for the p-type sample. This breakthrough technique is expected to be able to be applied to synthesize other borides also.

Methods

Commercially available YB_4 (99.9%, Japan New Metals Co., Ltd.), AlB_2 (Sigma-Aldrich Co., Ltd.), amorphous B (99%, New Metals and Chemicals Co., Ltd.) and AlF_3 (Wako Co., Ltd.) powders were used as the starting materials. YB_4 and AlB_2 were selected as the precursor for reactive sintering, and AlF_3 was selected as the sintering additive. The powders of YB_4, AlB_2, B and 0–1 wt.% AlF_3 were simply mixed under ethanol for 30 min using SiO_2 mortar with nominal compositions of $Y_{0.62}Al_yB_{14}$, where $y = 0.71$, 1.24, 1.55 and 1.86. For $y = 0.71$ (YA0 samples), five different sintering conditions were tested;10 min and 1 h under the uniaxial pressure of ~30 MPa, each with and without AlF_3, and 5 min under the uniaxial pressure of 80 MPa with AlF_3. Subsequent samples YA1, YA2 and YA3 were prepared with AlF_3 additive and 1 h sintering time. The excess amount of Al ($y = 1.24$–1.86) was used to prepare Al-rich n-type yittrium aluminoborides.

The powder mixtures were dried at 373 K for 3 h in an oven, and then poured into a 10 mm diameter graphite die. Here, graphite paper was used as a release agent. The mixtures were heated up to 1773 K in a SPS apparatus (Dr. Sinter, Fuji Denpa Koki Co., Ltd.) with heating rate of 100 K/min, and then reactively sintered at 1773 K for 5–60 min under uniaxial pressure of 28–80 MPa in a reduced-pressure Ar atmosphere (−0.03 MPa). After sintering, the samples were cooled down with cooling rate of 200 K/min, and finally, the sintered discs, 10 mm in diameter and ~2 mm in thickness, were obtained.

After sintering, as-sintered samples were slightly grinded by a diamond plate (#400) to remove the graphite paper on their surface. The densities of grinded samples were measured using Archimedes' method. The constituent phases of sintered samples were analyzed by X-ray diffraction (XRD, Smart lab 3, Rigaku) with Cu Kα radiation (λ=1.5418 Å). The XRD patterns were collected at $2\theta = 10$–90° with in a step of 0.01°. The compositions of the prepared $Y_xAl_yB_{14}$ samples by reactive SPS were estimated from Rietveld refinement using FullProf software. The thermal diffusivity of each sample was measured from 373 to 973 K by using a laser flash analysis apparatus (LFA, TC-7000, ADVANCE RIKO, Inc.). Prior to the LFA, the samples were coated with carbon. After LFA, samples were cleaned to remove the carbon on their surfaces, and then machined into bar-shaped specimens by cutting machine. The electrical resistivity and Seebeck coefficient of the specimens were evaluated from 373 to 973 K using a thermoelectric tester (ZEM-2, ADVANCE RIKO, Inc.). The distance between probes used for the measurements was 5.6 mm. The specific heat capacities of the samples were measured from 313–1073 K using a high temperature differential scanning calorimetry (STA449F3-NT24, NETZSCH Japan Co., Ltd.). As crucibles, Pt pans, Pt lids and Alumina liner were used. Microstructure of fracture surfaces of each sample was observed by scanning electron microscopy (SEM, S-4800, Hitachi High-Technologies Co.) at an acceleration voltage of 10.0 kV. To investigate the components of matrix and secondary phases on the fracture surface, energy-dispersive X-ray spectroscopy (EDX, Hitachi High-Technologies Co.) was used.

Received: 15 October 2019; Accepted: 5 May 2020;
Published online: 02 June 2020

References

1. Snyder, G. J. Thermoelectric Power Generation: Efficiency and compatibility. in *Thermoelectrics handbook*: *macro to nano* (ed. Rowe, D. M.) 9-1-26 (CRC Taylor and Francis, 2006).
2. Mori, T. Novel principles and nanostructuring methods for enhanced thermoelectrics. *Small* **13**, 1702013 (2017).
3. Mao, J. *et al*. Advances in thermoelectrics. *Adv. Phys.* **67**(2), 69–147 (2018).
4. Vaney, J.-B. *et al*. Magnetism-mediated thermoelectric performance of the Cr-doped bismuth telluride tetradymite. *Mater. Today Phys.* **9**, 100090 (2019).
5. Tsujii, N., Nishide, A., Hayakawa, J. & Mori, T. Observation of enhanced thermopower due to spin fluctuation in weak itinerant ferromagnet. *Sci. Adv.* **5**, eaat5935 (2019).
6. Mori, T. & Priya, S. Materials for energy harvesting: at the forefront of a new wave. *MRS Bull.* **43**, 176–180 (2018).
7. Akinaga, H., Fujita, H., Mizuguchi, M. & Mori, T. Focus on advanced materials for energy harvesting: prospects and approaches of energy harvesting technologies. *Sci. Tech. Adv. Mater.* **19**, 563–544 (2018).
8. Tian, R., Wan, C., Hayashi, N., Aoai, T. & Koumoto, K. Wearable and flexible thermoelectrics for energy harvesting. *MRS Bull.* **43**, 193–198 (2018).
9. Petsagkourakis, I. *et al*. Thermoelectric materials and applications for energy harvesting power generation. *Sci. Tech. Adv. Mater.* **19**, 836–862 (2018).
10. Mori, T. Perspectives of high-temperature thermoelectric applications and p-type and n-type aluminoborides. *JOM* **68**, 2673–2679 (2016).
11. Yazawa, K., Koh, Y. R. & Shakouri, A. Optimization of thermoelectric topping combined steam turbine cycles for energy economy. *Appl. Energy.* **109**, 1–9 (2013).
12. Yazawa, K. & Shakouri, A. Thermoelectric topping cycles with scalable design and temperature dependent material properties. *Scr. Mater.* **111**, 58–63 (2016).
13. Kuroki, T. *et al*. Waste heat recovery in steelworks using a thermoelectric generator. in *Proceedings of the 11th European Conference on* Thermoelectrics: ETC 2013 (eds. Amaldi, A. & Tang, F.) 143-149 (Springer, 2014).
14. Andrei, V., Bethke, K. & Rademann, K. Thermoelectricity in the context of renewable energy sources: joining forces instead of competing. *Energy Environ. Sci.* **9**, 1528–1532 (2016).

15. Lan, J.-L. *et al*. Enhanced thermoelectric performance of In_2O_3-based ceramics via nanostructuring and point defect engineering. *Sci. Rep.* **5**, 7783 (2015).
16. Mikami, M. & Ozaki, K. Thermoelectric properties of nitrogen-doped TiO_{2-x} compounds. *J. Phys.: Conf. Ser.* **379**, 012006 (2012).
17. Kovalevsky, A. V. *et al*. Towards a high thermoelectric performance in rare-earth substituted $SrTiO_3$: effects provided by strongly-reducing sintering conditions. *Phys. Chem. Chem. Phys.* **16**, 26946–26954 (2014).
18. Jood, P. *et al*. Al-doped zinc oxide nanocomposites with enhanced thermoelectric properties. *Nano Lett.* **11**, 4337–4342 (2011).
19. Michiue, Y. *et al*. Optical, and thermoelectric properties of $Ga_2O_3(ZnO)_9$. *RSC Adv.* **1**, 1788–1793 (2011).
20. Maki, R. S. S., Mitani, S. & Mori, T. Effect of spark plasma sintering (SPS) on the thermoelectric properties of magnesium ferrite. *Mater. Renew. Sustain. Energy* **6**(2), 1–8 (2017).
21. Ohkubo, I. & Mori, T. Anisotropic thermoelectric properties in layered complex nitrides with α-$NaFe_2O_2$-type structure. *APL Mater.* **4**, 104808 (2016).
22. Ohkubo, I. & Mori, T. Anisotropic anomalies of thermoelectric transport properties and electronic structures in layered complex nitrides AMN_2 (A = Na, Cu; M = Ta, Nb). *Chem. Mater.* **27**, 7265–7275 (2015).
23. Aselage, T. L., Emin, D., McCready, S. S. & Duncan, R. V. Large enhancement of boron carbides' Seebeck coefficients through vibrational softening. *Phys. Rev. Lett.* **81**, 2316 (1998).
24. Caruso, A. N. *et al*. Surface photovoltage effects on the isomeric semiconductors of boron-carbide. *Appl. Phys. Lett.* **84**, 1302 (2004).
25. Domnich, V., Reynaud, S., Haber, R. A. & Chhowalla, M. Boron carbide: structure, properties, and stability under stress. *J. Am. Ceram. Soc.* **94**, 3605–3628 (2011).
26. Rasim, K. *et al*. Local atomic arrangements and band structure of boron carbide. *Angew. Chem. Int. Ed.* **57**, 6130–6135 (2018).
27. Innocent, J.-L. *et al*. Thermoelectric properties of boron carbide/HfB_2 composites. *Mater. Renew. Sustain Energy* **6**(6), 1–7 (2017).
28. Nakayama, T., Shimizu, J. & Kimura, K. Thermoelectric properties of metal-doped β-rhombohedral boron. *J. Solid State Chem.* **154**, 13–19 (2000).
29. Sologub, O., Salamakha, L., Stöger, B., Michiue, Y. & Mori, T. Zr doped β-rhombohedral boron: widely variable Seebeck coefficient and structural properties. *Acta Mater.* **122**, 378–385 (2017).
30. Gong, Y. *et al*. Thermal conductivity and Seebeck coefficients of icosahedral boron arsenide films on silicon carbide. *J. Appl. Phys.* **108**, 084906 (2010).
31. Frye, C. D., Edgar, J. H., Ohkubo, I. & Mori, T. Seebeck coefficient and electrical resistivity of single crystal $B_{12}As_2$ at high temperature. *J. Phys. Soc. Jpn.* **82**, 095001 (2013).
32. Mori, T. High temperature thermoelectric properties of B_{12} icosahedral cluster-containing rare earth boride crystals. *J. Appl. Phys.* **97**, 093703 (2005).
33. Mori, T. *et al*. Effect of Zn doping on improving crystal quality and thermoelectric properties of borosilicides. *Dalton Trans.* **39**, 1027–1030 (2010).
34. Sussardi, A., Tanaka, T., Khan, A. U., Schlapbach, L. & Mori, T. Enhanced thermoelectric properties of samarium boride. *J. Materiomics* **1**, 196–204 (2015).
35. Mori, T. & Tanaka, T. Effect of transition metal doping and carbon doping on thermoelectric properties of YB_{66} single crystals. *J. Solid State Chem.* **179**, 2889–2894 (2006).
36. Takeda, M., Terui, M., Takahashi, N. & Ueda, N. Improvement of thermoelectric properties of alkaline-earth hexaborides. *J. Solid State Chem.* **179**, 2823–2826 (2006).
37. Gürsoy, M., Takeda, M. & Albert, B. High-pressure densified solid solutions of alkaline earth hexaborides (Ca/Sr, Ca/Ba, Sr/Ba) and their high-temperature thermoelectric properties. *J. Solid State Chem.* **221**, 191–195 (2015).
38. Mori, T. & Nishimura, T. Thermoelectric properties of homologous p- and n-type boron-rich borides. *J. Solid State Chem.* **179**, 2908–2915 (2006).
39. Berthebaud, D., Nishimura, T. & Mori, T. Microstructure and thermoelectric properties of dense $YB_{22}C_2N$ samples fabricated through spark plasma sintering. *J. Electron. Mater.* **40**, 682–686 (2011).
40. Mori, T., Nishimura, T., Schnelle, W., Burkhardt, U. & Grin, Y. The origin of the n-type behavior in rare earth borocarbide $Y_{1-x}B_{28.5}C_4$. *Dalton Transactions* **43**, 15048–15054 (2014).
41. Mori, T. Perspectives of high-temperature thermoelectric applications and *p*-type and *n*-type aluminoborides. *JOM* **68**, 2673–2679 (2016).
42. Korsukova, M. M., Lundstrom, T. & Tergenius, L.-E. The crystal structure of defective $YAlB_{14}$ and $ErAlB_{14}$. *J. Alloys Compd.* **187**, 39–48 (1992).
43. Maruyama, S., Miyazaki, Y., Hayashi, K., Kajitani, T. & Mori, T. Excellent p-n control in a high temperature thermoelectric boride. *Appl. Phys. Lett.* **101**, 152101 (2012).
44. Maruyama, S. *et al*. Al insertion and additive effects on the thermoelectric properties of yttrium boride. *J. Appl. Phys.* **115**, 123702 (2014).
45. Sahara, R. *et al*. Theoretical and experimental investigation of the excellent p-n control in yttrium aluminoborides. *Sci. Technol. Adv. Mater.* **15**, 035012 (2014).
46. Maruyama, S. *et al*. Microstructure and thermoelectric properties of $Y_xAl_yB_{14}$ samples fabricated through the spark plasma sintering. *Mater. Renew. Sustain Energy* **3**(31), 1–6 (2014).
47. Kim, B.-N. *et al*. Transparent hydroxyapatite ceramics consolidated by spark plasma sintering. *Scr. Mater.* **69**, 366–369 (2013).
48. Son, H.-W., Maki, R. S. S., Kim, B.-N. & Suzuki, Y. High-strength pseudobrookite-type $MgTi_2O_5$ by spark plasma sintering. *J. Ceram. Soc. Japan.* **124**, 1–3 (2016).
49. Guillon, O. *et al*. Field-assisted sintering technology/ spark plasma sintering: mechnisms, materials, and technology developments. *Adv. Eng. Mater.* **16**, 830–849 (2014).
50. Boucher, B. & Halet, J. F. Boron in solid-state chemistry: Some portraits of metal borides taken from a rich structural gallery. in *Handbook of Boron Science: With Applications in Organometallics, Catalysis, Materials and Medicine* (eds. Hosmane, N. S. & Eagling, R.) 159-188 (World Scientific, 2018).
51. Akopov, G., Pangilinan, L. E., Mohammadi, R. & Kaner, R. B. Perspective: Superhard metal borides: A look forward. *APL Mater.* **6**, 070901 (2018).
52. Müller, K. -H., Schneider, M., Fuchs, G. & Drechsler, S. -L. Rare-Earth Nickel Borocarbides. in *Handbook on the Physics and Chemistry of Rare Earths* (eds. Gschneidner, K. A. Jr., Bünzli, J. -C. G. & Pecharsky, V. K.) 175-336 (Elsevier, 2008).
53. Mori, T. Thermoelectric and magnetic properties of rare earth borides: Boron cluster and layered compounds. *J. Solid State Chem.* **275**, 70–82 (2019).
54. Mori, T. Higher Borides. In *Handbook on the Physics and Chemistry of Rare Earths* (eds. Gschneidner, K. A. Jr., Bünzli, J. -C. G. & Pecharsky, V. K.) 105-173 (Elsevier, 2008).
55. Son, H.-W., Kim, B.-N., Suzuki, T. S. & Suzuki, Y. Fabrication of translucent AlN ceramics with MgF_2 additive by spark plasma sintering. *J. Am. Ceram. Soc.* **101**, 4430–4433 (2018).
56. Mori, T., Nishimura, T., Yamaura, K. & Takayama-Muromachi, E. High temperature thermoelectric properties of a homologous series of *n*-type boron icosahedra compounds: A possible counterpart to *p*-type boron carbide. *J. Appl. Phys.* **101**, 093714 (2007).
57. Guse, W. & Saalfelds, H. X. X-ray characterization and structure refinement of a new cubic alumina phase (σ-Al_2O_3) with spinel-type structure. *N. Jb. Miner. Mn. H.* **5**, 217–226 (1990).

58. Mori, T. & Hara, T. Hybrid effect to possibly overcome the trade-off between Seebeck coefficient and electrical conductivity. *Scripta Mater.* **111**, 44–48 (2016).
59. Boyle, C. *et al*. Competing dopants grain boundary segregation and resultant seebeck coefficient and power factor enhancement of thermoelectric calcium cobaltite ceramics. *Ceram. Int.* **43**, 11523–11528 (2017).
60. Mott, N. F. Conduction in glasses containing transition metal ions. *J. Non-Cryst. Solids* **1**, 1–17 (1968).
61. Li, S. S. *Semiconductor Physical Electronics* (Springer, 2th edition, 2006).
62. Zvyagin, I. P. On the theory of hopping transport in disordered semiconductors. *Phys. Status. Solidi. B* **58**, 443–449 (1973).
63. Cox, J. D., Wagman, D. D. & Medvedev, V. A. CODATA key values for thermodynamics (Hemisphere Pub. Corp., 1989).
64. Lide, D. R. *CRC Handbook of Chemistry and Physics* (CRC Press, 84th edition, 2003).
65. Khan, A. U. *et al*. Nano-micro-porous skutterudites with 100% enhancement in ZT for high performance thermoelectricity. *Nano Energy* **31**, 152–159 (2017).
66. Ahmed, F., Tsujii, N. & Mori, T. Microstructure analysis and thermoelectric properties of iron doped CuGaTe2. J. Materiomics **4**, 221–227 (2018).
67. Hinterleitner, B. *et al*. Thermoelectric performance of a metastable thin-film Heusler alloy. *Nature* **576**, 85–90 (2019).
68. Ahmed, F., Tsujii, N. & Mori, T. Thermoelectric properties of CuGa1-xMnxTe2: power factor enhancement by incorporation of magnetic ion. *J. Mater. Chem. A* **5**, 7545–7554 (2017).

Acknowledgements

This work was supported by JSPS KAKENHI JP16H06441, JP17H02749 and CREST JPMJCR15Q6, JPMJCR19Q4. K.Y. was partly supported by JSPS KAKENHI grant number JP19K05643.

Author contributions

H.S. and T.M. wrote the main manuscript text, D.B. analyzed x-ray diffraction patterns, H.S. K.Y., A.Y., T.S. analyzed microstructure and impurity phases, K.S. measured thermal properties, H.S. measured thermoelectric properties and analyzed mechanical properties, T.M. and H.S. analyzed physical properties, H.S. prepared figures 1–15. All authors contributed to discussion and reviewed the manuscript.

Competing interests

The authors declare no competing interests.

Additional information

Supplementary information is available for this paper at https://doi.org/10.1038/s41598-020-65818-z.

Correspondence and requests for materials should be addressed to T.M.

Reprints and permissions information is available at www.nature.com/reprints.

Publisher's note Springer Nature remains neutral with regard to jurisdictional claims in published maps and institutional affiliations.